



Cite this: *J. Mater. Chem. C*, 2025, 13, 9705

Improving the memory window of a ferroelectric thin film transistor using an atomic layer deposited HfN_x interfacial layer†

Hyun Woo Nam,^{ab} Jae Hoon Lee,^a Seung Kyu Ryoo,^a Seong Jae Shin,^a Kun Hee Ye,^{ac} Kyung Do Kim,^a Seung yong Byun,^a In Soo Lee,^a Suk Hyun Lee,^a Jae Hee Song,^a Jung hae Choi^{id} and Cheol Seong Hwang^{id} *^a

This work examines the impact of atomic-layer-deposited 1-nm-thick HfN_x interfacial layer (IL) deposition and NH_3 annealing conditions on the ferroelectric properties of $\text{Hf}_{0.5}\text{Zr}_{0.5}\text{O}_2$ (HZO) thin film capacitors and ferroelectric thin-film transistors (FeTFTs) with an amorphous InGaZnO channel. Adjusting these processing parameters enabled significant improvements in key device performance metrics, including the memory window (MW) and data retention stability of the FeTFTs. The optimized NH_3 annealing process at 450 °C facilitated nitrogen diffusion into the HZO matrix, decreasing charge trap density and oxygen vacancies. This annealing condition decreased the remanent polarization and slightly increased the coercive field, yielding a maximum MW of ~ 1.9 V. A MW of ~ 1.0 V could be retained for up to 10 years. In contrast, the device without the optimized IL showed a MW of only ~ 0.6 V with a retention time shorter than ~ 1 year. These findings demonstrate the effectiveness of HfN_x IL deposition and NH_3 annealing for enhancing the performance and reliability of amorphous InGaZnO channel FeTFTs, making them promising candidates for nonvolatile memory applications. It also provides a viable method to independently control the remanent polarization and coercive field, which are conventionally deemed material-specific properties.

Received 3rd February 2025,
Accepted 1st April 2025

DOI: 10.1039/d5tc00453e

rsc.li/materials-c

1. Introduction

Ferroelectric thin film transistors (FeTFTs) are gaining greater interest as a memory device in the next-generation vertically-stacked flash memory.¹ As for the ferroelectric field-effect transistors (FeFETs) using bulk Si as the channel material, bistable or multi-stable ferroelectric (FE) polarizations of the FE materials, such as $\text{Hf}_{0.5}\text{Zr}_{0.5}\text{O}_2$ (HZO) thin films, are incorporated into the gate stack of the FeTFT. These polarizations control the electrical conductivity of the thin film channel layer, enabling nonvolatile memory.^{2–6} Recently, amorphous oxide semiconductors (AOSs), such as amorphous InGaZnO (a-IGZO), have attracted significant attention as the thin film channel layer due to their compatibility with the back end of the line

(BEOL) process and potential performance uniformity due to its amorphousness.^{7–9} Therefore, metal/FE/AOS structures, such as TiN/HZO/a-IGZO, deserve careful study as the crucial components in FeTFTs.^{10,11}

However, the FeTFTs and FeFETs generally encompass several issues related to their inherent material properties and device operation mechanisms. In the metal/FE/metal (MFM) capacitor structure, the metal layers' abundant carriers (electrons and holes) sufficiently compensate for the positive and negative FE-bound charges and induce little depolarization effect. In contrast, FeTFT and FeFET operate based on the field effect in the channel induced by the uncompensated FE-bound charge.^{12–16} Therefore, the depolarization field across the FE layer in the gate stack incurs data retention concerns.^{17,18} In many cases, this effect decreases the memory window (MW) of the FeTFT and FeFET, of which the uninterrupted value must be double the coercive voltage ($2V_c$) of the FE film.^{19,20} In FeTFT with the IGZO channel, the lack of inversion charges (holes) in the IGZO channel also destabilizes the FE polarization state where the negative end of the polarization heads toward the channel, further decreasing the MW.²¹

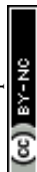
The recent theoretical work by Park *et al.*, using the quantitative simulation of the FE domain structure in the FeFET

^a Department of Materials Science and Engineering & Inter-University Semiconductor Research Center, College of Engineering, Seoul National University, Gwanak-ro 1, Gwanak-gu, Seoul 08826, Republic of Korea.
E-mail: cheolsh@snu.ac.kr

^b SK Hynix Semiconductor, Inc., Icheon, Gyeonggi 17336, Republic of Korea

^c Center for Electronic Materials, Korea Institute of Science and Technology, Seoul, 02792, Republic of Korea

† Electronic supplementary information (ESI) available. See DOI: <https://doi.org/10.1039/d5tc00453e>



structure, indicated that the spontaneous polarization (P_s) of the FE layer should not be too high so as not to induce a high depolarization field effect.¹⁹ Still, P_s must not be too low. Otherwise, the memory states cannot be discerned. Besides, the V_c must be as high as possible to ensure a large MW. Therefore, the desired polarization-voltage curve shape has low remanent polarization (P_r , $\sim 5 \mu\text{C cm}^{-2}$) and high V_c ($> 3 \text{ V}$), which is contradictory to the requirements for MFM capacitors for ferroelectric random access memory. However, this type of FE material rarely exists due to the general nature of FE materials. Hard FE materials have high P_r and high coercive field (E_c), such as recently reported $\text{Al}_{0.7}\text{Sc}_{0.3}\text{N}$ ($P_r > \sim 100 \mu\text{C cm}^{-2}$, $E_c > \sim 5 \text{ MV cm}^{-1}$),^{22–25} while soft FE materials have low P_r and high E_c , such as $\text{Pb}(\text{Zr,Ti})\text{O}_3$ ($P_r \sim 20\text{--}40 \mu\text{C cm}^{-2}$, $E_c \sim 0.1 \text{ MV cm}^{-1}$).^{26,27} HZO has properties between them ($P_r \sim 15\text{--}30 \mu\text{C cm}^{-2}$, $E_c \sim 1 \text{ MV cm}^{-1}$),²⁸ so increasing film thickness may increase the MW to the desired value. However, its metastability of the FE phase (orthorhombic phase with space group: $Pca2_1$) secures feasible ferroelectricity in this material at a specific thickness range ($\sim 5\text{--}15 \text{ nm}$).²⁹ When the film thickness increases over this range to increase the V_c , the film usually forms a non-polar monoclinic phase (m-phase, space group: $P2_1/c$), often decreasing the V_c .³⁰ Therefore, securing sufficient MW ($> 1 \text{ V}$ for single level and $> 6 \text{ V}$ for triple level cell) is challenging.

This work suggests a materials solution to this problem using the HfN_x interfacial layer (IL) between the heavily p-type doped Si (P^{++}Si) gate and HZO FE thin film. The recent work by Lee *et al.* elucidated that the P^{++}Si gate suppresses the unfavorable domain pinning of the HfO_2 -based FE film despite its interfacial SiO_2 layer formation in the a-IGZO-channel-based FeTFT.²¹ Therefore, this work adopts the P^{++}Si gate despite its interfacial SiO_2 layer formation.

The HfN_x IL was grown by a specific atomic layer deposition (ALD) process developed recently in the authors' group.³¹ The extremely high oxidation potential of Hf compared to its nitridation potential rendered the grown film always contaminated with high oxygen concentration (up to $\sim 40\%$) during the ALD process by the residual oxygen in the film growth chamber, even using the load-lock system. Ryoo *et al.* solved this problem by cyclic purging of the ALD chamber with Hf-precursor vapor before the onset of the ALD step.³¹ This specific ALD process decreased the residual oxygen concentration in the film to $\sim 20\%$ with a residual carbon concentration of $\sim 8\%$, but this is still a significant value. However, post-deposition annealing under NH_3 ambient by rapid thermal annealing (RTA) at 900°C decreased the oxygen and carbon concentrations below ~ 5 and 2% .³¹ Nonetheless, such a high RTA temperature is incompatible with the FeTFT process, which aims at compatibility with the BEOL process. Also, the ALD HfN_x layer has not been used as an IL in the FeTFT or FeFET.

Kim *et al.* reported the effects of HfN_x IL between the HZO film and TiN bottom electrode (BE) in the TiN/HZO/IL/TiN capacitor structure, where the reactive sputtering process grew $1\text{--}2 \text{ nm}$ -thick HfN_x , more precisely $\text{HfO}_{0.61}\text{N}_{0.72}$.³² They reported that the FE performance of the MFM capacitor was

significantly improved by effectively forming the o-phase with the smaller and more uniform grain size of the HZO film with less film defects, such as pinholes and nano-cracks. The authors reported that the proportion of the non-ferroelectric m-phase increases significantly, reducing the P_r and decreasing the ferroelectric properties when the IL thickness exceeds 2 nm .³² Therefore, the HfN_x IL thickness was fixed at 1 nm in this work. The IL was *in situ* oxidized during the $\sim 10\text{-nm}$ -thick HZO film ALD on top and formed a single-layer FE film with nitrogen doping. However, they did not report the NH_3 annealing effect or FeFET properties.³² Also, reactive sputtering has lower compatibility with the FeTFT fabrication process, which will eventually have a three-dimensional structure like the current vertical NAND flash devices.

Therefore, this study combines these two previous works, *i.e.*, adopts the ALD HfN_x IL and NH_3 annealing process, and examines the effects of HfN_x IL on the MFM, metal/FE/insulator/semiconductor (MFIS) capacitor structures, and FeTFT devices, where the sputtered-a-IGZO film comprises a semiconductor layer. Notably, it was identified that the HfN_x IL with the RTA at 450°C decreased the P_r of the 10-nm -thick HZO film due to the increased grain size (and thus the increased m-phase fraction). Interestingly, its E_c slightly increased, which contradicts the usual observation of decreasing E_c with decreasing P_r . This unexpected result was explained by the nitrogen doping effect on the switching barrier through the density functional theory (DFT) calculation. As a result of these favorable property combinations, the MW of the FeTFT device with a channel length (L_{ch}) of $5 \mu\text{m}$ and a channel width (W_{ch}) of $20 \mu\text{m}$ could be increased from $\sim 0.5 \text{ V}$ to 1.9 V by incorporating the optimal IL.

2. Results and discussion

2.1. Structural properties of ferroelectric HZO films with a HfN_x interfacial layer

First, the impacts of the HfN_x film on the structural properties of HZO films were analyzed. Fig. 1(a) and (b) shows the cross-section high-resolution transmission electron microscopy (HRTEM) images of the 10-nm -thick single-layer HZO film stack and a 9-nm -thick HZO/ 1-nm -thick HfN_x IL stack, respectively. The HfN_x IL was annealed at 800°C for 60 seconds under NH_3 ambient using the RTA method before the deposition of the HZO film to decrease the oxygen and carbon concentrations in the HfN_x film.³¹ Both samples were annealed at 450°C for 30 seconds, corresponding to post-metallization annealing (PMA), after depositing the TiN top electrode (TE). In the TiN/HZO/ HfN_x /TiN structure, distinct HfN_x IL was not detected, suggesting that the thin 1-nm -thick HfN_x IL may have oxidized and intermixed with the HZO film. These findings were consistent with previous studies, which reported that PMA facilitates the oxidation of HfN_x and the subsequent diffusion of nitrogen into the HZO matrix, resulting in structural and chemical continuity.³³ However, the distinction of o- and m-phase grains from the TEM images was improbable due probably to the overlapping of the grain images along the electron beam direction of the TEM work. Therefore,



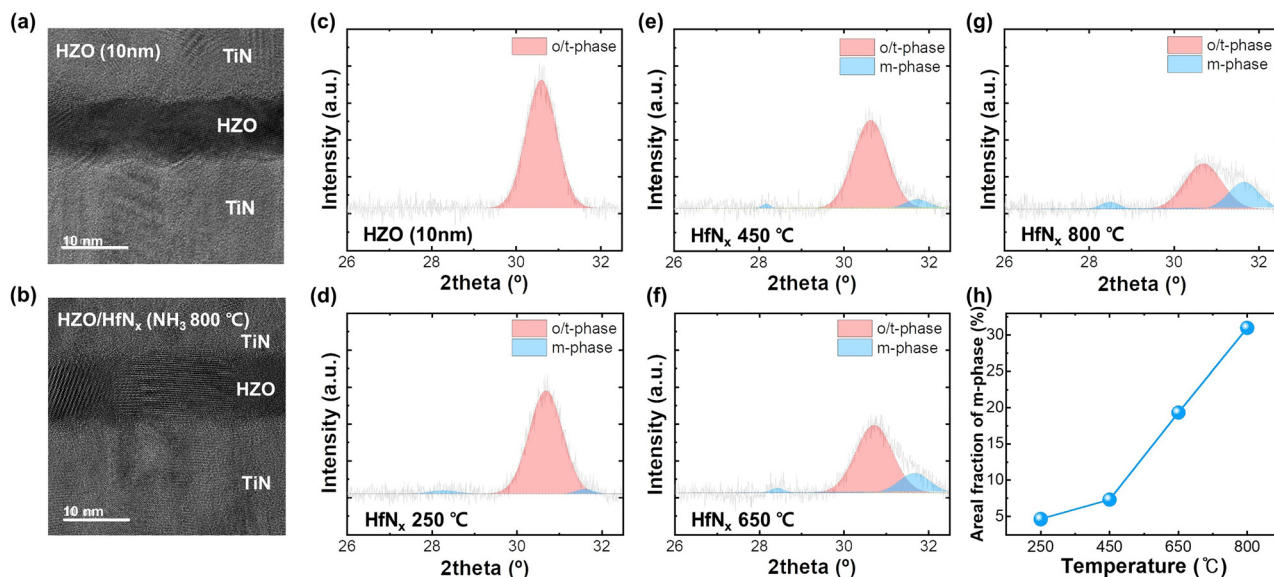


Fig. 1 The cross-sectional HRTEM images of (a) TiN/10-nm-thick HZO/TiN and (b) TiN/9-nm-thick HZO/1-nm-thick HfN_x films annealed in NH₃ at 800 °C/TiN. Both samples were annealed at 450 °C in N₂ gas for 30 seconds following the formation of the TE. Enlarged section (26–32.5°) of the GIXRD patterns, displaying the results for (c) the 10-nm-thick HZO sample and NH₃-annealed HfN_x (1-nm-thick) films at (d) 250 °C, (e) 450 °C, (f) 650 °C, and (g) 800 °C. The areas shaded in light red and light blue were identified as the o/t-phase and m-phase peaks, respectively, using Gaussian fitting. (h) Calculated m-phase areal fractions (%) corresponding to the conditions in (d) through (g).

grazing-angle incidence X-ray diffraction (GIXRD) was adopted to identify the phase evolution.

Fig. 1(c) shows the GIXRD pattern of the 10-nm-thick HZO film in the 2θ range with well-resolved o- and m-phase characteristic peaks. Fig. 1(d)–(g) show the GIXRD patterns of the 9-nm thick HZO/1-nm thick HfN_x films, where the annealing temperature of HfN_x IL was varied from 250 to 800 °C. All samples underwent a PMA process at 450 °C following the deposition of the TiN TE. To quantify these phase changes, GIXRD patterns between $2\theta = 26^\circ$ and $2\theta = 32.5^\circ$ were deconvoluted using the Gaussian function. Fig. S2(a) and (b) (ESI†) show the wide range θ – 2θ GIXRD data and overlapped peaks in the narrow 2θ range. As the NH₃ annealing temperature increased from 250 °C to 800 °C, the o/tetragonal (t)-phase peak at $2\theta = 30.6^\circ$ (indicated by the red background) diminished. In contrast, the m-phase peaks at $2\theta = 28.5^\circ$ and $2\theta = 31.8^\circ$ (indicated by the blue background) intensified. These trends suggest that the phase of the HZO film transformed from o/t-phase to m-phase as the IL annealing temperature increases. The m-phase fraction was determined using eqn (1):³⁴

$$\text{m-phase fraction} = \frac{A(111\text{m}) + A(-111\text{m})}{A(111\text{m}) + A(-111\text{m}) + A(111\text{o})} \quad (1)$$

where $A(111\text{o})$, $A(111\text{m})$, and $A(-111\text{m})$ are the respective peak areas at $2\theta \sim 30.6^\circ$, $\sim 28.5^\circ$, and $\sim 31.8^\circ$. Fig. 1(h) shows that the m-phase fraction increased from $\sim 5\%$ to $\sim 31\%$ as the annealing temperature increased from 250 °C to 800 °C, again demonstrating that the IL annealing temperature significantly affects the phase of the HZO film.

The effect of the HfN_x IL on the grain size of HZO film was investigated using scanning electron microscopy (SEM)

analysis. Fig. 2(a) and (b) show the surface morphology of a 10-nm thick HZO and 9-nm thick HZO/1-nm thick HfN_x film, where the HfN_x IL was NH₃ annealed at 800 °C. Both HZO films underwent RTA at 450 °C for 30 seconds to emulate the PMA condition without the TiN TE deposition. Depositing TiN TE and removing it after PMA is desirable for accurate grain size and phase identification. However, these steps damaged the top surface morphologies of the HZO layer, not allowing the appropriate SEM image acquisition. Nonetheless, the adopted experimental procedure could identify the grain size trend.

The 9-nm thick HZO/1-nm thick HfN_x film exhibited larger grains (~ 9.0 nm in average diameter) than the 10-nm-thick HZO film (~ 7.1 nm). Fig. 2(c) shows the variation of HZO grain diameter as a function of IL RTA temperature. The results indicate that the HZO grain size increased with higher IL annealing temperatures. Previous studies reported that it influences the stabilization of the o-phase in FE HZO films by affecting surface energy.^{35–38} Smaller grain sizes stabilize the o-phase, which has lower surface energy than the m-phase.^{39,40} Fig. 2(d) and (e) show the surface morphology of the TiN BE before and after NH₃ RTA at 800 °C, respectively. Fig. 2(f) shows the quantitative data of the average TiN grain diameter, indicating an increase from ~ 2.7 nm to ~ 3.3 nm by RTA. Fig. 2(g) and (h) show the surface morphology of the 10-nm-thick HfN_x film deposited on the TiN BE (the grain size of 1-nm-thickness was too thin to examine by SEM) before and after NH₃ RTA at 800 °C, respectively. Fig. 2(i) shows the quantitative analysis of the grain radius, indicating an increase from ~ 3.3 nm to ~ 4.9 nm after annealing. Therefore, when NH₃ RTA was applied to the HfN_x/TiN layer, the increase in grain size was more pronounced than that observed for the TiN BE alone. This



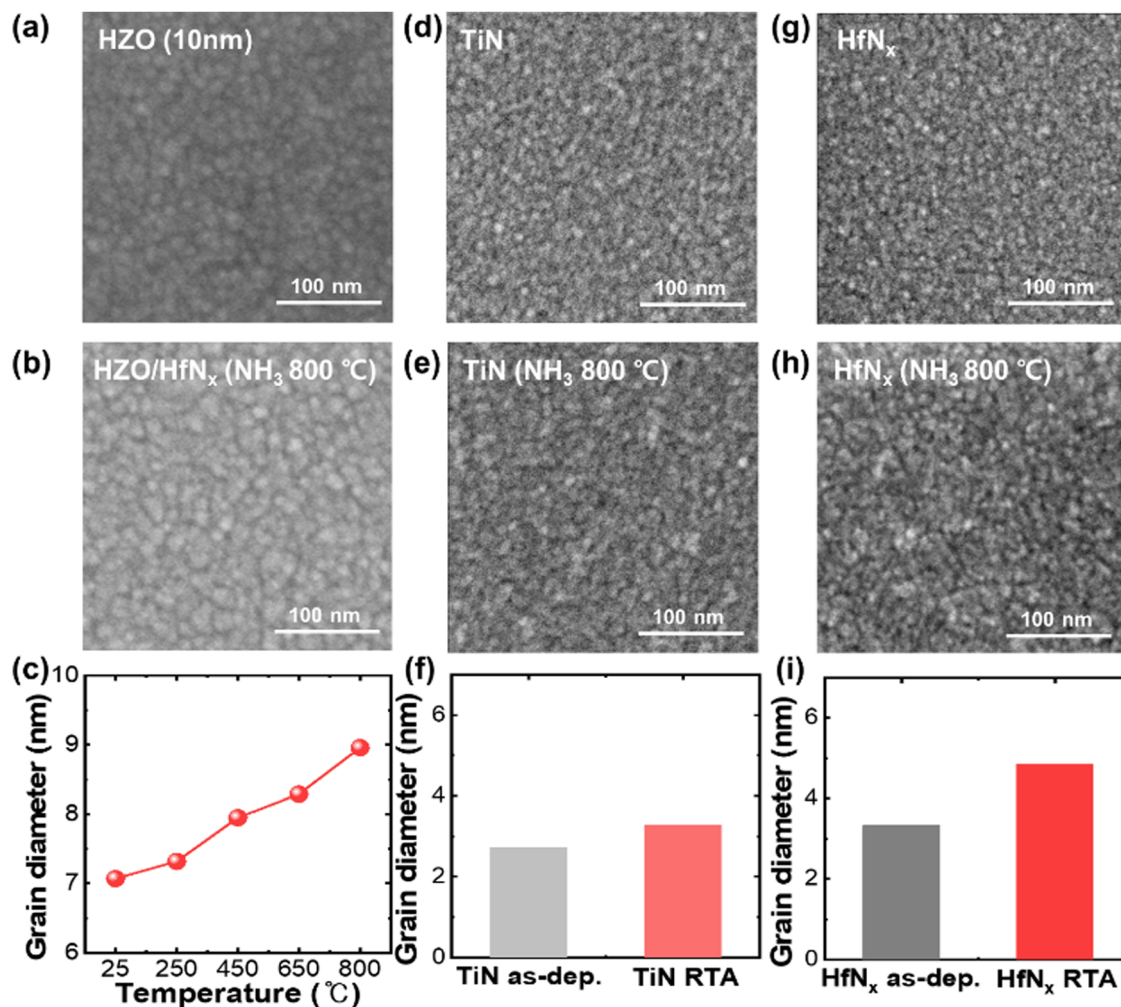


Fig. 2 SEM images and grain size analysis of HZO and TiN films with and without the HfN_x layer. (a) SEM image of a 10-nm-thick HZO sample and (b) a 9-nm-thick HZO/1-nm-thick HfN_x film annealed in NH₃ at 800 °C. (c) Average grain diameter of the without and with HfN_x samples annealed in NH₃ at various temperatures. (d) SEM image of a 50-nm-thick TiN film and (e) a 50-nm-thick TiN film annealed in NH₃ at 800 °C. (f) Average grain diameter corresponding to (d) and (e). (g) SEM image of a 10-nm-thick HfN_x film on TiN and (h) a 10-nm-thick HfN_x film annealed in NH₃ at 800 °C on TiN. (i) Average grain diameter corresponding to (g) and (h). Grain size analysis in (c), (f), and (i) was performed using the watershed method in Gwyddion software.

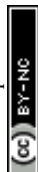
increased grain growth in the HfN_x/TiN layer promoted the grain growth of the HZO film and increased the m-phase fraction, as shown in Fig. 1(h).

2.2. Chemical and interfacial properties of HZO films with NH₃ annealing

Fig. 3 shows the variations in the film density (left y-axis) and roughness (right y-axis) of the 10-nm-thick HfN_x film achieved by X-ray reflectivity (XRR) and atomic force microscopy (AFM) (again, the 1-nm thickness was too thin to obtain accurate data) after NH₃ annealing at temperatures ranging from 250 °C to 800 °C. Fig. S3 (ESI[†]) shows the raw XRR and AFM data. The film density increased from $\sim 7.76 \text{ g cm}^{-3}$ at 250 °C to $\sim 9.03 \text{ g cm}^{-3}$ at 800 °C, corresponding to a 16% increase. This increase was attributed to the enhanced mobility of atoms at higher temperatures, which resulted in a denser atomic arrangement and decreased free volume within the film.⁴¹ Similarly, the

surface roughness (R_q) increased from $\sim 0.31 \text{ nm}$ at 250 °C to $\sim 0.73 \text{ nm}$ at 800 °C. This increase was attributed to the grain growth and non-uniform nitrogen diffusion into the film surface, a characteristic effect of NH₃ annealing.^{42,43}

Fig. 4(a) shows the deconvoluted X-ray photoelectron spectroscopy (XPS) Hf 4f spectrum of a TiN/5-nm-thick HZO/TiN stack after the PMA. The HZO layer thickness was decreased to 5 nm to improve the accuracy of nitrogen detection near the BE interface. The TiN TE was removed by wet-etching before the XPS analysis. The Hf-O bonds were observed at 18.7 eV and 17.0 eV binding energies, corresponding to 4f_{5/2} and 4f_{7/2}, respectively. Fig. 4(b) shows the deconvoluted XPS Hf 4f spectra of the TiN/5-nm-thick HZO/1-nm-thick HfN_x/TiN stack when the NH₃ annealing was performed at 250 °C after depositing the HfN_x IL. A decrease in the intensity of Hf-O bonds was observed (blue line), along with the appearance of Hf-N bond peaks at 17.8 eV and 16.9 eV (green line).^{44–47}



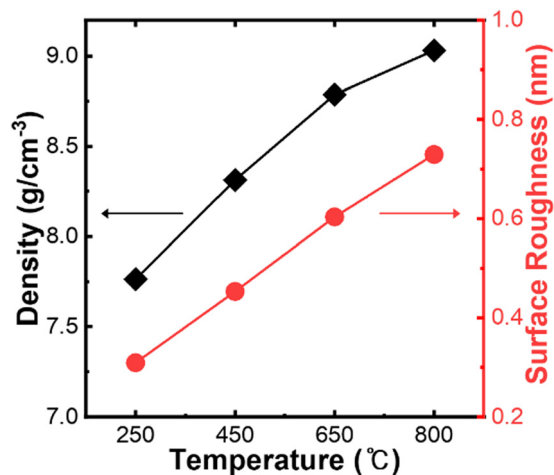


Fig. 3 Summary of density and surface roughness of 10-nm-thick HfN_x films annealed at NH₃ temperatures (250 °C to 800 °C).

Fig. 4(c) shows the deconvoluted XPS Hf 4f spectra of the TiN/5-nm-thick HZO/1-nm-thick HfN_x/TiN stack when the NH₃ annealing was performed at 800 °C after depositing the HfN_x IL. The increase in Hf–N bonding was more pronounced in this case than in others. The XPS results indicated that increasing the NH₃ annealing temperature of the HfN_x IL enhanced nitrogen incorporation into the HZO. Fig. S4 (ESI†) shows the proposed mechanism based on these findings. As the NH₃ annealing temperature increased from 250 °C to 800 °C, the oxygen concentration at the HfN_x surface decreased while the nitrogen concentration increased. During the subsequent HZO deposition and PMA processes, the diffused nitrogen facilitated the formation of Hf–N (or O–N) bonds and filled the oxygen vacancies (V_o) with nitrogen ions. The increased nitrogen concentration may also suppress the diffusion of V_o within the HZO layer.⁴⁸

2.3. Electrical performance and reliability of HZO films with and without a 1-nm-thick HfN_x interfacial layer

Fig. 5(a) shows the polarization–electric field (*P*–*E*) hysteresis curves, measured by the positive-up-negative-down (PUND) test with two triangular positive pulses and two triangular negative

pulses ($\pm 3.5 \text{ MV cm}^{-1}$), of TiN/10-nm-thick HZO/TiN and TiN/9-nm-thick HZO/1-nm-thick HfN_x/TiN capacitors, where the 1-nm-thick HfN_x IL underwent NH₃ RTA at temperatures ranging from 250 °C to 800 °C. The results indicated that the 10-nm-thick HZO sample exhibited the highest *P_r* value, while samples with the HfN_x IL showed gradually decreasing *P_r* with increasing NH₃ annealing temperature with the lowest *P_r* value when annealed at 800 °C. Fig. 5(b) shows the variation in *2P_r* and *2E_c* values derived from the *P*–*E* hysteresis curves in Fig. 5(a). The sample with no IL exhibited a *2P_r* value of $29.34 \mu\text{C cm}^{-2}$, while samples with the 1-nm-thick HfN_x IL showed a decrease in *2P_r* with increasing NH₃ annealing temperature. Specifically, the *2P_r* value decreased from $27.5 \mu\text{C cm}^{-2}$ at 250 °C to $4.07 \mu\text{C cm}^{-2}$ at 800 °C. Notably, the *2E_c* values slightly increased from 2.49 MV cm^{-1} at 250 °C to 2.68 MV cm^{-1} at 800 °C. These results deviate from the proportional relationship between *P_r* and *E_c* commonly observed in HfO₂-based films.⁴⁹ The decrease in *P_r* was attributed to the increased m-phase fraction within the HZO film, as indicated by the GIXRD results in Fig. 1(h), due to the promoted nitrogen diffusion and enhanced grain growth. The structural changes also affected the dielectric constant (ϵ_r), as shown in Fig. S5 (ESI†). Samples with HfN_x IL annealed in NH₃ exhibited a lower ϵ_r (~ 26 at 800 °C) than the 10-nm-thick HZO sample (~ 46). The observed decrease in ϵ_r was consistent with an increased m-phase fraction, further supporting the structural changes revealed by GIXRD in Fig. 1(h) and Fig. S2 (ESI†). Suppose the increased m-phase grains form a serially connected configuration with the o-phase grains along the out-of-plane direction. In that case, the *P_r* value must remain unvaried (or slightly increased), but the *E_c* value must be increased due to the tunnel-switch effect of the non-FE m-phase layer.⁵⁰ Therefore, the o/t-phase and m-phase most probably form a parallel configuration, and the FE o-phase property solely determines the *E_c* value. DFT calculation was performed to understand this effect, assuming that nitrogen incorporation increased the FE switching barrier in the HZO layer.

The DFT calculation evaluated the homogeneous switching barrier of a $2 \times 2 \times 2$ HfO₂ supercell containing a single oxygen vacancy coordinated with three Hf atoms (V_{o3}). The result was then compared to a similar structure where the V_{o3} was replaced by nitrogen, forming a vacancy substitution coordinated with

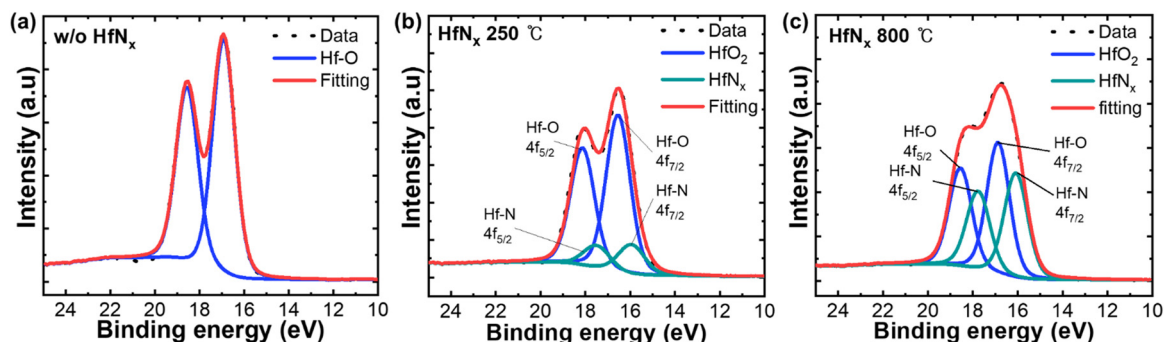


Fig. 4 Deconvoluted XPS Hf 4f spectrum of (a) a 5-nm-thick HZO film, and 5-nm-thick HZO/1-nm-thick HfN_x films annealed in NH₃ at (b) 250 °C and (c) 800 °C.



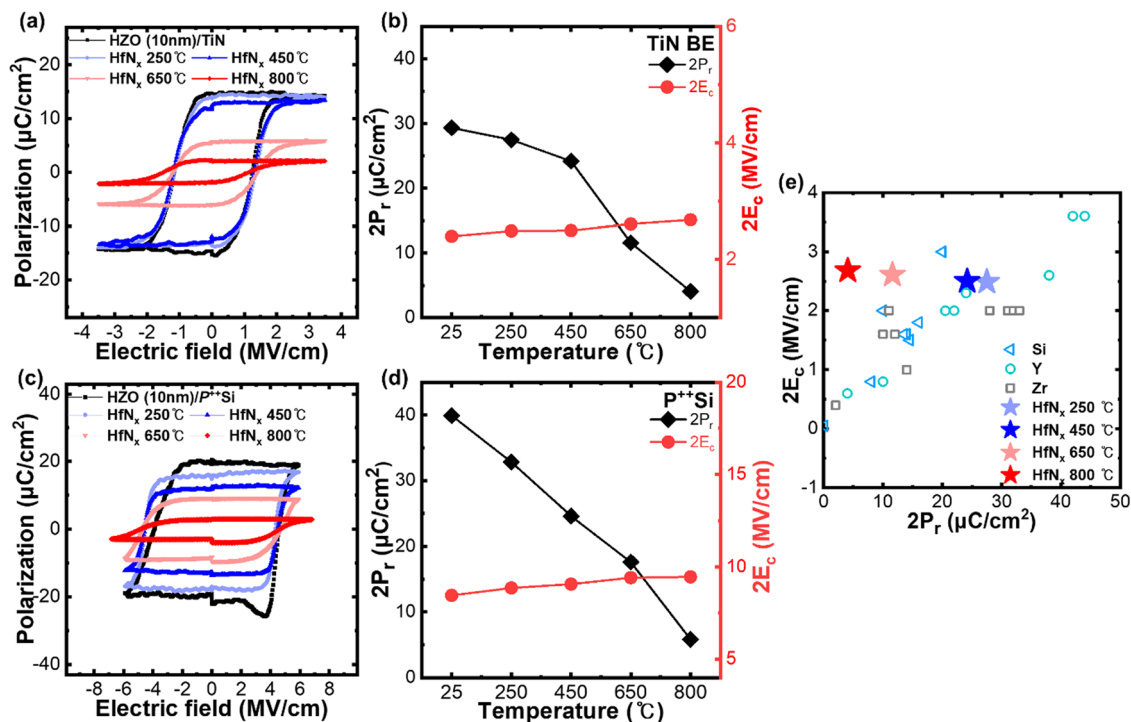


Fig. 5 (a) P - E curves of the TiN/10-nm-thick HZO/TiN sample and TiN/9-nm-thick HZO/1-nm-thick HfN_x/TiN films annealed in NH₃ at temperatures ranging from 250 °C to 800 °C. Measurements were conducted on MFM capacitors using the PUND method. (b) Summary of $2P_r$ and $2E_c$ values derived from the PUND measurements in (a). (c) P - E curves of TiN/10-nm-thick HZO/P⁺⁺Si and TiN/9-nm-thick HZO/1-nm-thick HfN_x/P⁺⁺Si MFIS capacitors were measured using the PUND method. (d) Summary of $2P_r$ and $2E_c$ values obtained from the PUND curves in (c). (e) P_r and E_c behavior results of HZO thin films with NH₃-annealed HfN_x IL and HfO₂ thin films with various dopants (Si, Y, Zr). The data for Si, Y, and Zr-doped films were taken from ref. 51–56.

three Hf atoms (N₀₃). Fig. S6 (ESI[†]) shows the DFT calculation results, demonstrating that N₀₃ increased the activation energy (E_a) of the switching barrier compared to V₀₃. The calculated E_a for N₀₃ was 4.16 eV per cell, higher than the 3.96 eV per cell for V₀₃. This increase in E_a was attributed to the structural changes induced by nitrogen incorporation. A V₀₃ created additional free space within the lattice, facilitating polarization switching by allowing easier movement.

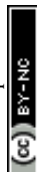
In contrast, when the N₀₃ filled V₀₃, the lattice became more constrained, making polarization switching sluggish. As a result, a higher electric field was required to overcome the barrier, and thus, a higher E_c must be induced. Therefore, the appropriate incorporation of nitrogen into the 9-nm-thick HZO film through the chemical interaction with the nitrogen-containing HfN_x IL decreases the P_r by forming parallel m-phase grains, while the E_c of the remaining o-phase slightly increases due to the higher switching barrier. It should be noted that the E_c of parallel m- and o-phase is solely determined by the FE o-phase. This finding corresponds to the desirable direction of the FeTFT device, as discussed above.

Fig. 5(c) shows the P - E hysteresis curves using PUND pulses of the MFIS capacitors with the TiN/10-nm-thick HZO/P⁺⁺Si and TiN/9-nm-thick HZO/1-nm-thick HfN_x/P⁺⁺Si structures described in Fig. S1(b) (ESI[†]). The measurements were performed at a 3.5 MV cm⁻¹ bias field strength and 1 kHz frequency, similar to the conditions used for the MFM case. The MFIS with no IL showed the highest P_r value, while samples with the HfN_x IL

showed a gradual decrease in P_r with increasing NH₃ annealing temperature. This trend was consistent with the behavior observed for the MFM capacitors. Fig. 5(d) shows the variation in $2P_r$ and $2E_c$ values derived from the PUND P - E hysteresis curves in Fig. 5(c). The sample with no IL exhibited a $2P_r$ value of 39.9 $\mu\text{C cm}^{-2}$. For samples with the 1-nm-thick HfN_x IL, the $2P_r$ value decreased from 32.8 $\mu\text{C cm}^{-2}$ at 250 °C to 5.8 $\mu\text{C cm}^{-2}$ at 800 °C. In contrast, the $2E_c$ values slightly increased from 8.45 MV cm⁻¹ for the no IL sample to 9.45 MV cm⁻¹ for the sample annealed at 800 °C. The estimated E_c values were higher for the samples on the P⁺⁺Si substrate than on the TiN substrate. This increase in E_c was attributed to the charge injection caused by the tunneling switch effect of the native oxide layer on the Si surface and partaking of the voltage by the finite accumulation and depletion layer thicknesses of the Si substrate.²¹

Fig. 5(e) shows the relationship between P_r and E_c for various doped-HfO₂ films in MFM configurations reported in the literature, including experimental data from this study. Si,^{51,52} Y,^{53,54} and Zr-doped HfO₂ films^{55,56} from other works exhibited a proportional relationship between P_r and E_c . In contrast, the samples with the NH₃-annealed HfN_x IL showed an unusual inverse P_r vs. E_c relationship (star symbols). This result demonstrated that P_r could be controlled independently of E_c , a behavior not typically observed in conventional FE materials.

Fig. 6(a) shows the endurance performance of the various MFM capacitors with a cycling electric field of 3.5 MV cm⁻¹ at 100 kHz. Samples with the HfN_x IL showed stable endurance



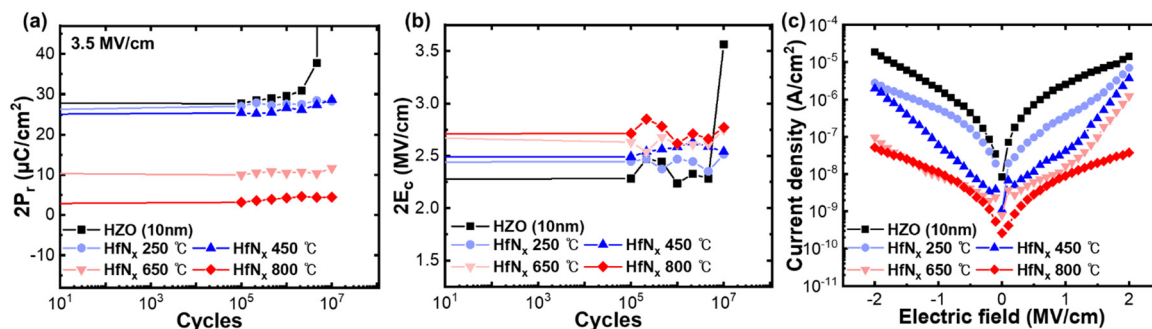


Fig. 6 Endurance test results of TiN/10-nm-thick HZO/TiN and TiN/9-nm-thick HZO/1-nm-thick HfN_x/TiN films annealed in NH₃ at 250 °C to 800 °C/TiN for the cycling field strengths of (a) 3.5 MV cm⁻¹ at the frequency of 100 kHz. (b) 2E_c values of endurance by NH₃ annealing temperature in (a). (c) J–E characteristics of the sample with no IL and TiN/9-nm-thick HZO/1-nm-thick HfN_x/TiN films annealed in NH₃ at 250 °C to 800 °C.

beyond 10⁷ cycles, while the single-layer HZO sample exhibited a hard breakdown before 10⁷ cycles. The improved endurance of the samples with HfN_x IL was attributed to the reduction in P_r and the decreased oxidation of the TiN BE. As P_r decreased, the charge displacement during polarization switching was decreased, thereby minimizing charge-induced defect formation within the HZO layer during cycling.^{57,58} Simultaneously, the HfN_x IL suppressed the formation of interfacial oxides (TiO_x or TiO_xN_y) on the TiN BE.³² As the NH₃ annealing temperature increased, nitrogen diffusion into the HZO layer further promoted m-phase formation, as shown in Fig. 1(h), contributing to P_r reduction and suppressing the adverse interfacial reaction. These combined effects further enhanced the endurance performance. Fig. 6(b) shows the variation in 2E_c under cycling conditions at 3.5 MV cm⁻¹. The samples with HfN_x IL exhibited stable 2E_c values regardless of cycling, consistent with the trends observed in Fig. 6. These results demonstrated that nitrogen incorporation was crucial for maintaining E_c values.

Fig. 6(c) shows the characteristics of the current density–electric field (J – E). The leakage current was significantly decreased in the samples with the HfN_x IL compared to the no IL sample. The sample with the HfN_x IL annealed at 800 °C in NH₃ recorded the lowest leakage current ($\sim 3.7 \times 10^{-8}$ A cm⁻² at 2.0 MV cm⁻¹), while the no IL sample exhibited a much higher leakage current ($\sim 1.5 \times 10^{-5}$ A cm⁻² at 2.0 MV cm⁻¹). Without the HfN_x IL, the TiN electrode likely forms interfacial oxides, such as TiO_x or TiO_xN_y, by taking oxygen atoms from the HZO layer. These oxides negatively impacted the TiN/HZO interface, and the induced V_o in the HZO layer degraded the FE reliability of the HZO film. This observation was consistent with the findings reported by Kim *et al.*³² Overall, the NH₃ annealing diminished the adverse interfacial reaction and improved the film performance.

2.4. Improved memory performance of a-IGZO channel FeTFTs through an HfN_x interfacial layer and NH₃ annealing

After the 1-nm-thick HfN_x IL was deposited and NH₃ annealing was performed, the P_r of the HZO layer was found to decrease while E_c slightly increased, as discussed in Section 3.3. Park *et al.* previously reported that achieving an optimal P_r was

essential for retaining the threshold voltage (V_{th}) shift or MW close to 2V_c.¹⁹ The results in the previous section indicate that HZO films with an HfN_x IL can be more suitable for FeTFT structures, although they are less desirable for MFM capacitor applications. Fig. S1(c) (ESI[†]) shows a schematic diagram of the a-IGZO FeTFT fabrication, incorporating HfN_x IL and HZO layers on a P⁺⁺Si bottom gate (G). In the operational behavior of a-IGZO FeTFTs, the n-type nature of a-IGZO was found to limit the electric field distribution within the channel. In program mode, the P⁺⁺Si gate was positively biased, and the accumulated electrons in the a-IGZO layer fluently compensated for the positive FE-bound charge at the HZO/a-IGZO interface, turning the channel on, resulting in a low V_{th} . Conversely, the P⁺⁺Si gate was negatively biased in erase mode, and the negative FE-bound charge must be located near the HZO/a-IGZO interface. However, the limited hole generation in the n-type a-IGZO inversion charges could not fluently compensate for the negative FE-bound charge. Instead, V_o and the laterally spreading electric field from the source and drain (S and D) electrodes compensated the negative FE-bound charge.⁵⁹

Fig. 7(a)–(e) shows the transfer characteristics of a-IGZO FeTFTs, presenting the drain current–gate voltage (I_D – V_G) on the left y-axis and transconductance (g_m) on the right y-axis as functions of V_G . The FE gate stack consists of (a) a 10-nm-thick HZO and (b)–(e) a 9-nm-thick HZO film deposited on a 1-nm-thick HfN_x IL, annealed at 250, 450, 650, and 800 °C, respectively, in an NH₃ atmosphere. All FeTFT devices exhibited I_D – V_G curves with counterclockwise hysteresis, coinciding with the FE switching, except for the sample annealed at 800 °C. The V_G sweep range was set to –4.5 V to +4.5 V for the sample in (a) and –5.5 V to +5.5 V for the other samples because the sample in (a) showed breakdown at voltages exceeding 4.5 V.

The MW of the HZO films in the a-IGZO FeTFT structure was determined from the I_D – V_G curves measured during forward and backward voltage sweeps.⁶⁰ First, the g_m was derived from the I_D – V_G curves by differentiating the I_D for the V_G , following eqn (2). The maximum transconductance value ($g_{m,max}$) was determined during the forward and backward sweeps, and the corresponding gate voltages for these maxima were determined: $V_{g_{m,max}}^{fwd}$ for the forward sweep and $V_{g_{m,max}}^{bwd}$ for the backward sweep. At each $V_{g_{m,max}}$ point, a tangent line on the



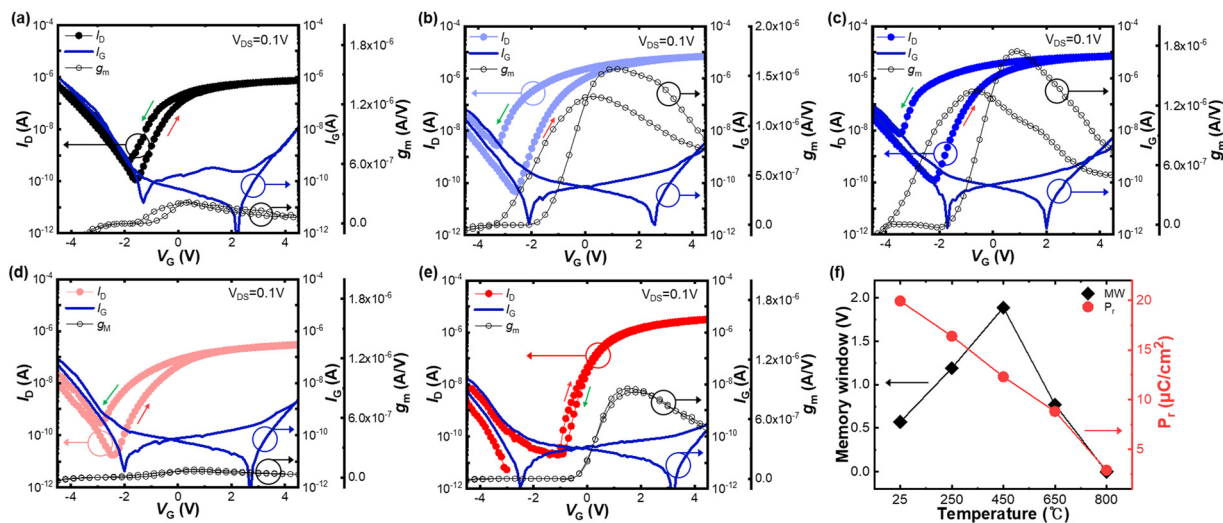


Fig. 7 Transfer curve (I_D - V_G , I_G - V_G , and g_m - V_G) of the a-IGZO TFTs with ferroelectric HZO. (a) 10-nm-thick HZO, and (b)–(e) 9-nm-thick HZO film deposited on a 1-nm-thick HfN_x IL annealed in NH_3 at (b) 250 °C, (c) 450 °C, (d) 650 °C, and (e) 800 °C. (f) Summary of MW and P_r values for the 10-nm-thick HZO sample and with 1-nm-thick HfN_x IL at NH_3 annealing temperatures (250–800 °C).

I_D - V_G curves was used to determine the x -intercept, accurately representing the voltage shift. Finally, MW was calculated as the difference between the x -intercepts ($V_{x\text{-int}}$) of the forward and backward sweeps, as shown in eqn (3):

$$g_m = \partial I_D / \partial V_G \quad (2)$$

$$\text{Memory window (MW)} = V_{x\text{-int}}^{\text{fwd}} - V_{x\text{-int}}^{\text{bwd}} \quad (3)$$

The calculated MW of the sample without the IL was 0.57 V. In contrast, the MW values for the samples with the 1-nm-thick HfN_x IL varied with the NH_3 annealing temperature. The MW increased to 1.19 V at 250 °C to a peak value of 1.89 V at 450 °C, then decreased to 0.77 V at 650 °C. At 800 °C, a charge-trap-like phenomenon (clockwise hysteresis) was observed. Besides, the gate leakage current (I_G)- V_G curves (navy lines) showed a butterfly shape, confirming the FE nature of the gate insulator stack,^{61,62} with the sample containing 1-nm-thick HfN_x IL exhibiting lower I_G , indicating the lowest defect concentration. This behavior is consistent with the leakage observed in the MFM structure shown in Fig. 6(c). The high I_D observed in the highly negative bias region coincided with the I_G , indicating that it is not due to the ambipolar conduction behavior of the a-IGZO channel.

Fig. 7(f) shows the relationship between MW and P_r (reproduced from Fig. 5(d)) for the a-IGZO FeTFTs. From no IL device to the device with IL annealed at 450 °C, the MW increases while P_r decreases. This behavior could be ascribed to the decreased depolarization effect of the FE film with lower P_r as the IL annealing temperature increased to 450 °C. However, further increasing the IL annealing temperature decayed the P_r to below $\sim 10 \mu\text{C cm}^{-2}$, which again decreased the MW due to too small P_r .

Still, the MW of the a-IGZO TFT structure was observed to be smaller than $2V_c$ even at the optimized condition. This reduction was attributed to ineffective charge compensation

at the FE/a-IGZO interface. The n-type nature of a-IGZO limited the availability of inversion charges, leading to incomplete polarization switching, thereby reducing the MW.^{20,21} A summary of the MW, leakage current, and endurance characteristics is provided in Table 1 for comparison.

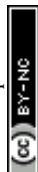
Fig. 8 shows the room-temperature retention characteristics of the FeTFT with (a) no IL and (b)–(d) with IL annealed at temperatures of 250 °C, 450 °C, and 650 °C, respectively. Retention measurements were not performed for the 800 °C sample due to the absence of a measurable MW. The MW of the sample in (a) was expected to last less than one year, while the MW of the HfN_x IL sample was expected to last longer. Among them, the sample annealed at 450 °C demonstrated the most stable retention, with the predicted MW of ~ 1.0 V maintained after 10 years. These results demonstrated that NH_3 annealing at 450 °C minimized charge trapping, enabling the FeTFT device to ensure reliable and stable data storage over extended periods, which is crucial for nonvolatile memory applications.

3. Experimental sections

A 50-nm-thick TiN BE was deposited on a 100-nm-thick SiO_2/Si substrate using DC sputtering (ENDURA 5500, Applied

Table 1 Comparison of MW (a-IGZO TFT), leakage current (MFM), and endurance (MFM) characteristics with and without a 1-nm-thick HfN_x IL under NH_3 annealing temperatures

Sample	Memory window (V)	Leakage current (A cm^{-2})	Endurance (cycles)
10-nm-thick HZO (without HfN_x)	0.57	$\sim 1.5 \times 10^{-5}$	10^6
HfN_x 250 °C	1.19	$\sim 7.0 \times 10^{-6}$	$> 10^7$
HfN_x 450 °C	1.89	$\sim 3.6 \times 10^{-6}$	$> 10^7$
HfN_x 650 °C	0.77	$\sim 1.2 \times 10^{-6}$	$> 10^7$
HfN_x 800 °C	0	$\sim 3.7 \times 10^{-8}$	$> 10^7$



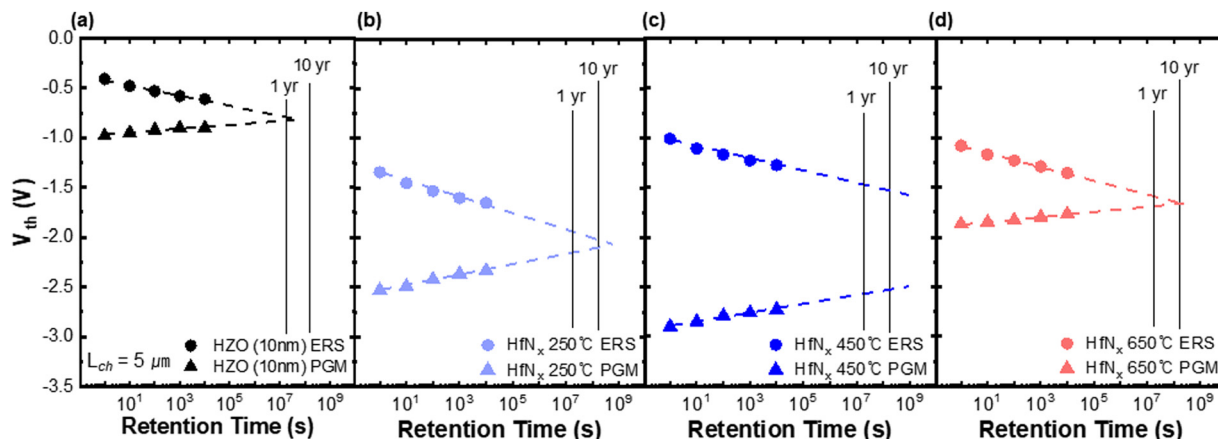


Fig. 8 Data retention characteristics of (a) HZO-based IGZO FeTFTs (10-nm-thick HZO layer) and devices incorporating 1-nm-thick HfN_x IL annealed in NH₃ at (b) 250 °C, (c) 450 °C, and (d) 650 °C.

Materials, USA). Subsequently, a 1-nm-thick HfN_x IL was deposited on the TiN/SiO₂/Si substrate using thermal ALD (Atomic Classic, CN-1) with tetrakis-ethylmethylaminohafnium (Hf[N(C₂H₅)CH₃]₄, TEMA-Hf) as the Hf precursor and NH₃ gas as the N-source, following the specific chamber purge conditions mentioned above.³¹ The bubbler-type TEMA-Hf canister and gas line were maintained at 65 °C and 100 °C, respectively. The precursor was carried by the Ar carrier gas at a flow rate of 950 standard cubic centimeters per minute (sccm), which was also used as the purge gas. The flow rate of NH₃ gas was 50 sccm. The optimized ALD sequence was TEMA-Hf pulse (5 s) – Ar purge (60 s) – NH₃ pulse (0.5 s) – Ar purge (60 s), which was repeated for 10 cycles to grow a 1-nm-thick HfN_x film. The HfN_x films were post-deposition annealed in an NH₃ atmosphere using a rapid thermal process (RTP, Real RTP-100, ULTECH) at temperatures ranging from 250 to 800 °C for 60 s. Annealing for 30 s under similar conditions was insufficient for improving the ferroelectric performances. After the RTP, all HZO films were deposited using another thermal ALD system (Atomic Classic, CN-1) at a substrate temperature of 280 °C. To ensure a consistent total thickness across all samples, the HfN_x inserted samples were fabricated with a 1-nm-thick HfN_x IL and a 9-nm-thick HZO layer. In contrast, the sample without HfN_x used a 10-nm-thick HZO layer. The total stack thickness was maintained at 10 nm for all samples. TEMA-Hf and tetrakis-ethylmethylaminozirconium (Zr[N(C₂H₅)CH₃]₄, TEMA-Zr) were used as Hf- and Zr-precursors, respectively, and O₃ (180 g m⁻³ density) as the oxygen source. The ALD sequence was TEMA-Hf, Zr pulse (0.8, 1.4 s) – Ar purge (30 s) – O₃ pulse (5 s) – Ar purge (10 s). For the electrical characterization, a 50-nm-thick TiN TE was deposited at room temperature using RF sputtering (SRN-120, SORONA Inc.). During the TE deposition process, a shadow mask with an opening diameter of ~300 μm was used for defining the capacitor area. After fabricating the TiN/HZO/HfN_x/TiN capacitors, the PMA process was conducted at 450 °C for 30 s in an N₂ atmosphere at 110 Torr to crystallize the HZO film. Also, a P⁺⁺Si substrate with a resistivity of less than 0.005 Ω cm was employed as the BE in the MFIS structure,

replacing the TiN BE. The same deposition procedures were followed for MFIS sample fabrication. The FeTFT also adopted the P⁺⁺Si substrate as the bottom gate material.

To fabricate FeTFTs, 1-nm-thick HfN_x IL was deposited on the P⁺⁺Si bottom gate and NH₃-annealed at temperatures from 250 °C to 800 °C, followed by 9-nm-thick HZO thin film deposition. Then, a 20-nm-thick a-IGZO layer was deposited on the HZO at room temperature using RF magnetron sputtering (SRN-120, SORONA Inc.). The films were annealed at 400 °C for 30 s in an N₂ atmosphere *via* RTA to crystallize the HZO layer. Subsequently, a 50 nm-thick TiN film was deposited using RF sputtering (SRN-120, SORONA Inc.), and TiN source/drain electrodes were patterned to achieve a *W*_{ch} of 20 μm and a *L*_{ch} of 5 μm. The PMA was performed at 350 °C in a furnace to enhance contact with the a-IGZO channel and repair deposition-induced damage. Fig. S1 (ESI[†]) shows the schematic diagram of the fabrication steps for FE HZO devices on TiN thin-film electrodes and P⁺⁺Si substrates.

The film compositions were measured using X-ray fluorescence (XRF, Quant'X, Thermo SCIENTIFIC), and the microstructure of the fabricated samples was analyzed using HRTEM (JEM-2100F, JEOL). The crystallinity and phases of the HfN_x and HZO thin films were analyzed using GIXRD (X'pert Pro, PANalytical) with an angle of incidence = 0.5°. Bulk film density was estimated using XRR (X'pert Pro, PANalytical). The chemical bonding states and composition of the HfN_x and HZO films were evaluated using XPS (Versaprobe III, PHI). The topography and grain configuration of the films were analyzed using AFM (NX10, Park Systems) and SEM (SIGMA, Carl Zeiss). The grain sizes of the HZO and HfN_x films were quantified and statistically analyzed from plane-view SEM images using the watershed method in Gwyddion software.

DFT calculations were carried out using the Vienna Ab initio Simulation Package,^{63,64} applying the local density approximation^{65,66} combined with Blöchl's projector augmented wave method.^{67,68} A plane-wave energy cutoff of 600 eV was employed, and Γ -centered *k*-point meshes of 4 × 4 × 4 were used for the 2 × 2 × 2 supercells of orthorhombic HfO₂. The



atomic positions were relaxed until the Hellmann–Feynman forces were reduced to below $0.02 \text{ eV } \text{\AA}^{-1}$. The energy barrier for switching was determined using the nudged elastic band method with fixed lattice constants for the $2 \times 2 \times 2$ supercells.⁶⁹

For electrical characterization, P – E curves were measured using a ferroelectric tester (TF Analyzer 2000, Aixacct system) with a triangular bipolar pulse at 1 kHz. PUND tests were also performed to extract accurate P_r values free from leakage current interference. All P – E curve results were obtained after wakeup (cycling of 10^5 with an amplitude of 3.5 MV cm^{-1} at a frequency of 100 kHz). J – E characteristics of the HZO films were evaluated using a picoammeter (HP4140D, Hewlett Packard). Additionally, a semiconductor parameter analyzer (SPA, 4145B, Hewlett Packard) was used to measure the I_D – V_G , I_G – V_G , and retention characteristics of the FeTFTs.

4. Conclusions

This study investigated the effects of ALD HfN_x IL insertion and NH_3 annealing on the properties of the HZO-film-based MFM and MFIS capacitors and FeTFTs with an a-IGZO channel. A 1-nm-thick HfN_x IL was adopted for the capacitor structures between the 9-nm-thick HZO film and BEs (TiN or P^{++}Si). The $2P_r$ values of the HZO were observed to decrease with increasing NH_3 annealing temperatures, while the $2E_c$ values slightly increased. The decreased $2P_r$ could be ascribed to the increased m-phase fraction due to the larger grain size of the HZO film when it was grown on high-temperature annealed HfN_x IL. The $2E_c$ values are solely determined by the o-phase grains in the film, and the nitrogen diffusion into the HZO film increased the switching barrier of the o-phase HZO. DFT calculation supported this conclusion.

The FeTFT with no IL showed inappropriate MW ($\sim 0.57 \text{ V}$) and retention performance (< 1 year) due to too high P_r (invoking a strong depolarization effect) and high leakage current of the HZO film. In contrast, the 450°C NH_3 annealing condition for the 1-nm-thick HfN_x IL was confirmed to achieve the highest MW of $\sim 1.89 \text{ V}$ in FeTFT devices. The appropriate incorporation of the nitrogen enhanced the resistance to performance degradation by charge injection, meaning that the MW of $\sim 1.0 \text{ V}$ was retained for up to 10 years. Other conditions with higher P_r , due to high depolarization, and lower P_r , due to too low bound charge effect, degraded the MW and retention performances.

Therefore, interposing the 1-nm-thick HfN_x IL and NH_3 annealing at 450°C was a feasible method to enhance the FE and memory performance of a-IGZO FeTFTs. This study provides a notable strategy to decouple the P_r and E_c , which is usually unachievable in conventional FE film technology.

Author contributions

H. W. Nam designed and conducted the experiments and wrote the manuscript. J. H. Lee, S. J. Shin, K. D. Kim, S. K. Ryoo, and

K. H. Ye helped plan the experiments and analyze data. S. Y. Byun, I. S. Lee, S. H. Lee, J. H. Song and J. H. Choi reviewed the manuscript. C. S. Hwang supervised the whole research experiments and manuscript preparation.

Data availability

The data supporting this article have been included as part of the ESI.† The data that support the findings of this study are available from the corresponding author upon reasonable request.

Conflicts of interest

The authors declare they have no conflict of interest.

Acknowledgements

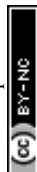
This work was supported by the National Research Foundation of Korea (no. 2020R1A3B2079882).

Notes and references

- 1 K. Florent, M. Pesic, A. Subirats, K. Banerjee, S. Lavizzari, A. Arreghini, L. Di Piazza, G. Potoms, F. Sebaai and S. McMitchell, In 2018 IEEE Int. Electron Devices Meet., 2018, pp. 2–5.
- 2 J. Müller, E. Yurchuk, T. Schlösser, J. Paul, R. Hoffmann, S. Müller, D. Martin, S. Slesazek, P. Polakowski and J. Sundqvist, In 2012 Symp. VLSI Technol., 2012, pp. 25–26.
- 3 S. Dünkler, M. Trentzsch, R. Richter, P. Moll, C. Fuchs, O. Gehring, M. Majer, S. Wittek, B. Müller and T. Melde, In 2017 IEEE Int. Electron Devices Meet., 2017, pp. 19–27.
- 4 M. H. Park, H. J. Kim, Y. J. Kim, W. Jeon, T. Moon and C. S. Hwang, *Phys. Status Solidi RRL*, 2014, **8**, 532–535.
- 5 M. Pešić, S. Knebel, K. Cho, C. Jung, J. Chang, H. Lim, N. Kolomiets, V. V. Afanas'ev, T. Mikolajick and U. Schroeder, *Solid-State Electron.*, 2016, **115**, 133–139.
- 6 W. Weinreich, A. Shariq, K. Seidel, J. Sundqvist, A. Paskaleva, M. Lemberger and A. J. Bauer, *J. Vac. Sci. Technol., B: Nanotechnol. Microelectron.: Mater., Process., Meas., Phenom.*, 2013, **31**, 01A109.
- 7 M. K. Kim and J. S. Lee, *Nano Lett.*, 2019, **19**, 2044–2050.
- 8 Y. Kato, Y. Kaneko, H. Tanaka and Y. Shimada, *Jpn. J. Appl. Phys.*, 2008, **47**, 2719–2724.
- 9 D. Kim, Y. R. Jeon, B. Ku, C. Chung, T. H. Kim, S. Yang, U. Won, T. Jeong and C. Choi, *ACS Appl. Mater. Interfaces*, 2021, **13**, 52743–52753.
- 10 F. Mo, Y. Tagawa, C. Jin, M. Ahn, T. Saraya, T. Hiramoto and M. Kobayashi, *IEEE J. Electron Devices Soc.*, 2020, **8**, 717–723.
- 11 F. Mo, T. Saraya, T. Hiramoto and M. Kobayashi, *Appl. Phys. Express*, 2020, **13**, 074005.
- 12 S. Miller and P. McWhorter, *J. Appl. Phys.*, 1992, **72**, 5999–6010.



- 13 F. Preisach, Über die Magnetische Nachwirkung, *Z. Med. Phys.*, 1935, **94**, 277–302.
- 14 T. Kamei, E. Tokumitsu and H. Ishiwara, *Trans. Inst. Electron., Inf. Commun. Eng., Sect. E*, 1998, **81**, 577–583.
- 15 H. T. Lue, C. J. Wu and T. Y. Tseng, *IEEE Trans. Electron Devices*, 2002, **49**, 1790–1798.
- 16 J. M. Sallese and V. Meyer, *IEEE Trans. Electron Devices*, 2004, **51**, 2145–2153.
- 17 T. Ma and J. P. Han, *IEEE Electron Device Lett.*, 2002, **23**, 386–388.
- 18 C. Black, C. Farrell and T. J. Licata, *Appl. Phys. Lett.*, 1997, **71**, 2041–2043.
- 19 H. W. Park, J. G. Lee and C. S. Hwang, *Nano Select*, 2021, **2**, 1187–1207.
- 20 T. Ando, *Materials*, 2012, **5**, 478–500.
- 21 J. H. Lee, Y. Lee, J. K. Han, K. D. Kim, S. R. Byun, H. W. Park and C. S. Hwang, *Adv. Electron. Mater.*, 2024, 2400516.
- 22 S. Fichtner, N. Wolff, F. Lofink, L. Kienle and B. Wagner, *J. Appl. Phys.*, 2019, **125**, 114103.
- 23 D. Drury, K. Yazawa, A. Zakutayev, B. Hanrahan and G. Brennecke, *Micromachines*, 2022, **13**, 887.
- 24 S. K. Ryoo, K. D. Kim, H. W. Park, Y. B. Lee, S. H. Lee, I. S. Lee, S. Byun, D. Shim, J. H. Lee and H. Kim, *Adv. Electron. Mater.*, 2022, **8**, 2200726.
- 25 K. D. Kim, S. K. Ryoo, H. S. Park, S. Choi, T. W. Park, M. K. Yeom and C. S. Hwang, *J. Appl. Phys.*, 2024, **136**, 024101.
- 26 J. G. Scott and C. A. PazDeAraujo, *Science*, 1989, **246**, 1400–1405.
- 27 H. R. Kim, S. H. Jeong, C. B. Jeon, O. S. Kwon, C. S. Hwang, Y. K. Han, D. Y. Yang and K. Y. Oh, *J. Mater. Res.*, 2001, **16**, 3583–3591.
- 28 J. Müller, T. Böske, D. Bräuhäus, U. Schröder, U. Böttger, J. Sundqvist, P. Kücher, T. Mikolajick and L. Frey, *Appl. Phys. Lett.*, 2011, **99**, 112901.
- 29 M. H. Park, Y. H. Lee, H. J. Kim, T. Schenk, W. Lee, W. Do, K. Kim, F. P. Fengler, T. Mikolajick, U. Schroeder and C. S. Hwang, *Nanoscale*, 2017, **9**, 9973–9986.
- 30 M. H. Park, Y. H. Lee, H. J. Kim, Y. J. Kim, T. Moon, K. D. Kim, S. D. Hyun and C. S. Hwang, *ACS Appl. Mater. Interfaces*, 2018, **10**, 42666–42673.
- 31 S. K. Ryoo, B. Y. Kim, Y. B. Lee, H. W. Park, S. H. Lee, M. Oh, I. S. Lee, S. Y. Byun, D. S. Shim and J. H. Lee, *J. Mater. Chem. C*, 2023, **11**, 8018–8026.
- 32 B. Y. Kim, H. W. Park, S. D. Hyun, Y. B. Lee, S. H. Lee, M. Oh, S. K. Ryoo, I. S. Lee, S. Byun and D. Shim, *Adv. Electron. Mater.*, 2022, **8**, 2100042.
- 33 B. Y. Kim, S. H. Kim, H. W. Park, Y. B. Lee, S. H. Lee, M. Oh, S. K. Ryoo, I. S. Lee, S. Byun and D. Shim, *Appl. Phys. Lett.*, 2021, **119**, 122902.
- 34 M. H. Park, J. H. Kim, Y. J. Kim, W. Lee, T. Moon and C. S. Hwang, *Appl. Phys. Lett.*, 2013, **102**, 242905.
- 35 K. Ishikawa, K. Yoshikawa and N. Okada, *Phys. Rev. B: Condens. Matter Mater. Phys.*, 1988, **37**, 5852–5856.
- 36 K. Nanda, A. Maisels, F. Kruis, H. Fissan and S. Stappert, *Phys. Rev. Lett.*, 2003, **91**, 106102.
- 37 F. D. Fischer, T. Waitz, D. Vollath and N. K. Simha, *Prog. Mater. Sci.*, 2008, **53**, 481–527.
- 38 B. Medasani, Y. H. Park and I. Vasiliev, *Phys. Rev. B: Condens. Matter Mater. Phys.*, 2007, **75**, 235436.
- 39 C. Xu, Y. Song, L. Lu, C. Cheng, D. Liu, X. Fang, X. Chen, X. Zhu and D. Li, *Nanoscale Res. Lett.*, 2013, **8**, 1–7.
- 40 S. Turteltaub and A. Suiker, *Int. J. Solids Struct.*, 2006, **43**, 7322–7336.
- 41 J. Thakur, R. Naik, V. Naik, D. Haddad, G. Auner, H. Lu and W. Schaff, *J. Appl. Phys.*, 2006, **99**, 023504.
- 42 H. Hopoğlu, H. Aydınoglu, A. Özer and E. Ş. Tüzemen, *Opt. Mater.*, 2021, **122**, 111685.
- 43 D. Dastan, K. Shan, A. Jafari, F. Gity, X. T. Yin, Z. Shi, N. D. Alharbi, B. A. Reshi, W. Fu and Ş. Tölu, *Appl. Phys. A: Mater. Sci. Process.*, 2022, **128**, 400.
- 44 S. Karwal, M. Verheijen, B. Williams, T. Faraz, W. Kessels and M. Creatore, *J. Mater. Chem. C*, 2018, **6**, 3917–3926.
- 45 A. Perry, L. Schlapbach and W. Sproul, *Solid State Commun.*, 1987, **62**, 23–26.
- 46 A. Arranz and C. Palacio, *Surf. Sci. Spectra*, 2004, **11**, 33–42.
- 47 W. Wang, T. Nabatame and Y. Shimogaki, *Surf. Sci.*, 2005, **588**, 108–116.
- 48 D. R. Hsieh, C. C. Lee and T. S. Chao, *IEEE Trans. Electron Devices*, 2022, **69**, 2074–2079.
- 49 J. D. Anderson, J. Merkel, D. Macmahon and S. K. Kurinec, *IEEE J. Electron Devices Soc.*, 2018, **6**, 525–534.
- 50 Q. Jiang, H. J. Lee, G. H. Kim and C. S. Hwang, *Adv. Mater.*, 2009, **21**, 2870–2875.
- 51 P. D. Lomenzo, P. Zhao, Q. Takmeel, S. Moghaddam, T. Nishida, M. Nelson, C. M. Fancher, E. D. Grimley, X. Sang and J. M. LeBeau, *J. Vac. Sci. Technol., B: Nanotechnol. Microelectron.: Mater., Process., Meas., Phenom.*, 2014, **32**, 03D123.
- 52 P. D. Lomenzo, Q. Takmeel, C. M. Fancher, C. Zhou, N. G. Rudawski, S. Moghaddam, J. L. Jones and T. Nishida, *IEEE Electron Device Lett.*, 2015, **36**, 766–768.
- 53 S. Starschich, D. Griesche, T. Schneller, R. Waser and U. Böttger, *Appl. Phys. Lett.*, 2014, **104**, 202903.
- 54 T. Olsen, U. Schröder, S. Müller, A. Krause, D. Martin, A. Singh, J. Müller, M. Geidel and T. Mikolajick, *Appl. Phys. Lett.*, 2012, **101**, 082905.
- 55 M. H. Park, H. J. Kim, Y. J. Kim, Y. H. Lee, T. Moon, K. D. Kim, S. D. Hyun, F. Fengler, U. Schroeder and C. S. Hwang, *ACS Appl. Mater. Interfaces*, 2016, **8**, 15466–15475.
- 56 M. G. Kozodaev, A. G. Chernikova, E. V. Korostylev, M. H. Park, R. R. Khakimov, C. S. Hwang and A. M. Markeev, *J. Appl. Phys.*, 2019, **125**, 034101.
- 57 T. Onaya, T. Nabatame, M. Inoue, T. Sawada, H. Ota and Y. Morita, *APL Mater.*, 2022, **10**, 051110.
- 58 K. Bao, J. Liao, F. Yan, S. Jia, B. Zeng, Q. Yang, M. Liao and Y. Zhou, *ACS Appl. Electron. Mater.*, 2023, **5**, 4615–4623.
- 59 D. Das, H. Park, Z. Wang, C. Zhang, P. V. Ravindran, C. Park, N. Afroze, P. K. Hsu, M. Tian and H. Chen, In 2023 Int. Electron Devices Meet., 2023, pp. 1–4.
- 60 Y. Swami and S. Rai, *J. Nanotechnol.*, 2017, **2017**, 4678571.



- 61 M. M. Hasan, C. W. Ahn, T. H. Kim and J. Jang, *Appl. Phys. Lett.*, 2021, **118**, 152901.
- 62 Y. Li, R. Liang, J. Wang, Y. Zhang, H. Tian, H. Liu, S. Li, W. Mao, Y. Pang and Y. Li, *IEEE J. Electron Devices Soc.*, 2017, **5**, 378–383.
- 63 G. Kresse and J. Furthmüller, *Phys. Rev. B: Condens. Matter Mater. Phys.*, 1996, **54**, 11169–11186.
- 64 G. Kresse and J. Furthmüller, *Comput. Mater. Sci.*, 1996, **6**, 15–50.
- 65 D. M. Ceperley and B. J. Alder, *Phys. Rev. Lett.*, 1980, **45**, 566–569.
- 66 J. P. Perdew and A. Zunger, *Phys. Rev. B: Condens. Matter Mater. Phys.*, 1981, **23**, 5048–5079.
- 67 G. Kresse and D. Joubert, *Phys. Rev. B: Condens. Matter Mater. Phys.*, 1999, **59**, 1758–1775.
- 68 P. E. Blöchl, *Phys. Rev. B: Condens. Matter Mater. Phys.*, 1994, **50**, 17953–17979.
- 69 D. Sheppard, P. Xiao, W. Chemelewski, D. D. Johnson and G. A. Henkelman, *J. Chem. Phys.*, 2012, **136**, 074103.

